Journal of Nuclear Medicine, published on November 18, 2021 as doi:10.2967/jnumed.121.262668

Title:

Total-Body PET Multiparametric Imaging of Cancer Using a Voxel-wise Strategy of Compartmental Modeling

Running title:

Total-Body PET Multiparametric Imaging

Authors:

Guobao Wang[1], Lorenzo Nardo[1], Mamta Parikh[2], Yasser G. Abdelhafez[1], Elizabeth Li[3], Benjamin A. Spencer[3,1], Jinyi Qi[3], Terry Jones[1], Simon R. Cherry[3,1], Ramsey D. Badawi[1,3]

Affiliations:

1. Department of Radiology, University of California Davis Medical Center, Sacramento, CA 95817, U.S.A
2. UC Davis Comprehensive Cancer Center, Sacramento, CA 95817, U.S.A
3. Department of Biomedical Engineering, University of California at Davis, Davis, CA 95616, U. S. A.

First author and corresponding author: Guobao Wang, Department of Radiology, University of California, Davis. 4860 Y Street, Sacramento, CA 95817. Email: gbwang@ucdavis.edu. Phone: 916-734-6537.

Word count: 5300

Figures: 7 (supplemental figures: 6)

Tables: 3

ABSTRACT

Quantitative dynamic PET with compartmental modeling has the potential to enable multiparametric imaging and more accurate quantification as compared to static PET imaging. Conventional methods for parametric imaging commonly use a single kinetic model for all image voxels and neglect the heterogeneity of physiological models, which can work well for single-organ parametric imaging but may significantly compromise total-body parametric imaging on long axial field-of-view scanners. In this paper, we evaluate the necessity of voxel-wise compartmental modeling strategies, including time delay correction and model selection, for total-body multiparametric imaging. **Methods**: Ten subjects (5 patients with metastatic cancer and 5 healthy volunteers) were scanned on the uEXPLORER total-body PET/CT system following injection of 370 MBq ^{18}F-fluorodeoxyglucose (FDG). Dynamic data were acquired for 60 minutes. Total-body parametric imaging was performed using two approaches. One is the conventional method that uses a single irreversible two-tissue compartmental model with and without time delay correction. The second approach selects the best kinetic model from three candidate models for individual voxels. The differences between the two approaches were evaluated for parametric imaging of micro kinetic parameters and FDG net influx rate K_i. **Results:** Time delay correction had a non-negligible effect on kinetic quantification of various organs and lesions. The effect was larger in lesions with higher blood volume. Parametric imaging of K_i with the standard two-tissue model introduced artifacts in vascular regions, which was overcome by the voxel-wise model selection strategy. **Conclusions**: The time delay and appropriate kinetic model vary in different organs and lesions. Modeling of the time delay of the blood input function and model selection improved total-body multiparametric imaging.

INTRODUCTION

Positron emission tomography (PET) allows dynamic scanning to monitor the spatiotemporal distribution of a radiotracer in the living body. With tracer kinetic modeling (e.g., compartmental models or graphical methods (*1*)), dynamic PET allows quantification of kinetic parameters in regions of interest (ROIs) and voxel-wise (i.e., parametric imaging) (*2*,*3*). PET parametric imaging has the potential to improve tumor contrast, derive meaningful biological measures of tracer transport and binding, and enable quantitative assessment of tumor response to cancer treatment as compared to standardized uptake value (SUV)(*4*). As the axial length of conventional PET scanners commonly ranges from 15 cm to 30 cm, clinical studies using dynamic PET have typically been limited to a restricted axial field-of-view which can only cover single organs or specific tumor locations. Whole-body implementation of parametric imaging has been pursued using conventional PET scanners but is mainly limited to the simplified Patlak graphical method (*5*-*7*), which is computationally efficient but does not explore the full potential of kinetic modeling for multiparametric imaging.

The advent of extended long axial field-of-view PET scanners such as the uEXPLORER (*8*-*10*), the PennPET Explorer (*11*,*12*) and the Siemens Quadra (*13*) is providing a paradigm shift for dynamic imaging. The longest of these has an axial field-of-view of 194 cm, providing not just unprecedented photon detection sensitivity but also simultaneous dynamic imaging and parametric imaging of the entire body (*9*,*14*). Image-derived input functions (IDIF) can also be obtained from the left ventricle or the aorta. Metastatic lesions that are widely separated can now be imaged at the same time with total-body PET. The objective of this work is to conduct a pilot clinical study to test the feasibility of multiparametric imaging with compartmental modeling in total-body dynamic PET.

A typical approach for PET parametric imaging is to apply a single model for all voxels in the image (*6*,*14*,*15*). This can be appropriate for conventional single-organ parametric imaging but becomes insufficient for total-body parametric imaging in which organ and tissue appropriate models are required. In this paper, we evaluated a voxel-wise compartmental modeling strategy for total-body PET multiparametric imaging.

METHODS

Total-body Dynamic PET/CT Image Acquisition

Ten subjects, including five patients with metastatic genitourinary cancer and five healthy volunteers, were recruited into this study at the University of California (UC) Davis Medical Center. Prior Ethics Committee and

Institution Review Board approval and informed consent were obtained. Patients were enrolled and scanned before the initialization of targeted therapy or immunotherapy. All subjects fasted for at least 6 hours before the study.

PET/CT imaging was performed on the uEXPLORER total-body system at the UC Davis EXPLORER Molecular Imaging Center. Each subject had a total-body CT scan from head to toe with arms down, followed by a 60-minute dynamic PET scan using an injection of approximately 370 MBq (10 mCi) ^{18}F-FDG. List-mode data were acquired and binned into 29 frames: 6×10s, 2×30s, 6×60s, 5×120s, 4×180s, 6×300s. Each frame was reconstructed into an image of size 150×50×486 with 4×4×4 mm^3 voxels using the vendor implementation of the time-of-flight ordered-subset expectation maximization algorithm with 4 iterations and 20 subsets. Standard corrections, including normalization, attenuation correction, deadtime correction, decay correction, random correction and scatter correction, were all applied (*10*).

Compartmental Modeling and Parametric Imaging

Lesion Selection and ROI Placement. For each scan, regions of interest (ROIs) were placed in various organs and on suspicious lesions to extract regional time activity curves (TACs). Up to five target lesions (maximum two per organ) were identified per scan. The lesion ROIs were defined using 41% of the maximum SUV (at 60 minutes post injection) in each lesion (*16*). An additional ROI was placed in the ascending aorta using both early-frame and late-frame images as guidance to extract an IDIF $\mathrm{C_{IDIF}(t)}$. Lesion delineation was performed using the AMIDE software (*17*).

Compartmental Models. The commonly used irreversible two-tissue (2T) compartmental model (*1*) (Fig. 1A) was used to model the dynamic FDG-PET data. The corresponding ordinary differential equation of this 2T model is:

$$\frac{\mathrm{d}}{\mathrm{d}t}\begin{bmatrix} C_\mathrm{f}(t) \\ C_\mathrm{m}(t) \end{bmatrix} = \begin{bmatrix} -(k_2+k_3) & 0 \\ k_3 & 0 \end{bmatrix}\begin{bmatrix} C_\mathrm{f}(t) \\ C_\mathrm{m}(t) \end{bmatrix} + \begin{bmatrix} K_1 \\ 0 \end{bmatrix} C_\mathrm{p}(t) \quad (1)$$

where $C_\mathrm{p}(t)$ is the FDG concentration in the plasma, $C_\mathrm{f}(t)$ is the concentration of free FDG and $C_\mathrm{m}(t)$ is the concentration of metabolized tracer in the tissue space at time t. The constant K_1 is the rate of FDG delivery from the plasma to the tissue space in units of mL/min/cm^3 (*18*); k_2 (min^{-1}) is the rate constant of tracer exiting the tissue space; k_3 (min^{-1}) is the rate constant of FDG being phosphorylated. This irreversible model assumes the dephosphorylation process is negligible (i.e., $k_4 = 0$). The total concentration of FDG in the extravascular space is

$$C_\mathrm{ev}(t) = C_\mathrm{f}(t) + C_\mathrm{m}(t) = H(t;\boldsymbol{\kappa}) \otimes C_\mathrm{p}(t), \quad (2)$$

where $\boldsymbol{\kappa} = [\,K_1, k_2, k_3]^T$ and $H(t;\boldsymbol{\kappa})$ is the impulse response function defined by

$$H(t;\boldsymbol{\kappa}) = \frac{K_1 k_3}{k_2+k_3} + \frac{K_1 k_2}{k_2+k_3} e^{-(k_2+k_3)t}. \quad (3)$$

The macro parameters K_i (net influx rate) and V_0 (initial volume of distribution) can be calculated by (*5*,*19*),

$$K_\mathrm{i} = \frac{K_1 k_3}{k_2+k_3}, V_0 = \frac{K_1 k_2}{(k_2+k_3)^2}. \quad (4)$$

The total radioactivity that can be measured by PET is modeled as the sum of the time courses of FDG in the vascular and extravascular spaces (Fig. 1B),

$$C_\mathrm{T}(t) = (1 - v_\mathrm{b}) C_\mathrm{ev}(t) + v_\mathrm{b} C_\mathrm{b}(t), \quad (5)$$

where v_b (ml/mL) is the fractional blood volume and $C_\mathrm{b}(t)$ represents the whole blood.

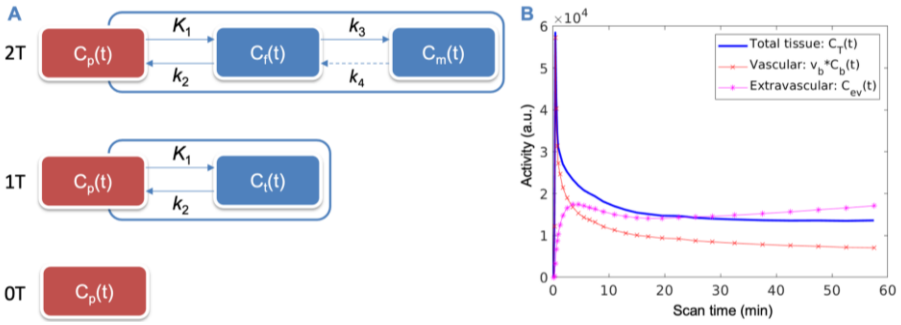

FIGURE 1: Compartmental modeling of ^{18}F-FDG. (A) 2-tissue (2T) model and reduced 1-tissue (1T) and no-tissue, blood volume model (0T); (B) illustration of the time courses of FDG in the vascular and extravascular spaces that constitute the total tissue TAC.

Modeling of Voxel-wise Time-delay in IDIF. Time delay exists between where the IDIF is extracted and the arrival of the radiotracer in the tissue of interest. Within the limited axial field-of-view of conventional PET scanners, the time-delay effect has been commonly neglected because of the short distance between an IDIF and tissue ROIs, especially if the temporal resolution is low (e.g., 20-40 s per frame). Accounting for the time delay has conventionally only been considered necessary for fast kinetics when relatively high temporal sampling is used (*20*,*21*). A recent example is shown by Feng *et. al.* (*22*) for fast total-body imaging of early FDG kinetics. In this paper, while the dynamic scan uses a standard temporal resolution (10 s/frame), we noted the long distance between the ascending aorta and distant lesions, as well as potentially high vascular contributions in some lesions. Hence, the time-delay effect is explicitly modeled in the blood input to each voxel by

$$C_\mathrm{T}(t) = (1 - v_\mathrm{b}) H(t;\boldsymbol{\kappa}) \otimes C_\mathrm{p}(t - t_\mathrm{d}) + v_\mathrm{b} C_\mathrm{b}(t - t_\mathrm{d}), \quad (6)$$

with the time delay parameter t_{d} to be jointly estimated with other kinetic parameters though the TAC fitting of a voxel. We postulate that time-delay correction has a higher impact on kinetic quantification if the fractional blood volume v_{b} is larger in the tissue, because the increased fraction of the vascular time course in turn influences the estimate of the extravascular time course $C_{\mathrm{ev}}(t)$, as projected from Fig. 1B.

Fitting Optimization and Setting. A measured TAC $\check{C}_{\mathrm{T}}(t)$ is fitted with the model TAC $C_{\mathrm{T}}(t)$ using a nonlinear least-square formulation:

$$\widehat{\boldsymbol{\theta}} = \arg\min_{\boldsymbol{\theta}} RSS(\boldsymbol{\theta}),\ RSS(\boldsymbol{\theta}) = \sum_{m=1}^{M} w_m\left[\check{C}_{\mathrm{T}}(t_{\mathrm{m}}) - C_{\mathrm{T}}(t_m)\right]^2, \tag{7}$$

where $RSS(\boldsymbol{\theta})$ denotes the residual sum of squares of the curve fitting. $\boldsymbol{\theta}$ is the unknown parameter set. For the irreversible 2T model, $\boldsymbol{\theta} = [\, v_{\mathrm{b}}, K_1, k_2, k_3, t_{\mathrm{d}}]^T$. t_m is the mid-point of the m^{th} frame in a total of M frames, and w_m is the weight for frame m. Given our interest in both K_{i} and K_1, a uniform weight was used as suggested by prior studies (*23*-*25*) (also demonstrated in supplemental Fig. 1).

The classic Levenberg-Marquardt algorithm with 50 iterations was used to solve the optimization problem in a similar way to our other work (*26*) and was implemented using C/C++ programming. The initial values of $\boldsymbol{\kappa}$ and v_{b} were set to $[0.01, 0.01, 0.01]^T$ and 0.01. The lower bound was zero and the upper bound was $[5.0, 5.0, 1.0]^T$ and 1.0, respectively. Time delay t_{d} was jointly estimated by a grid search with the lower and upper bounds set to -10s and 50s, respectively.

Table 1. List of models used for dynamic FDG-PET kinetic modeling

Model order	Number of unknown parameters, *n*	Kinetic parameters to be estimated
2T	5	v_{b}, K_1, k_2, k_3, t_{d}
1T	4	v_b, K_1, k_2, t_{d}
0T	2	v_b, t_{d}

Voxel-wise Model Selection. Conventionally for simplicity, parametric imaging uses a single kinetic model (e.g., the irreversible 2T model) for all voxels. In total-body parametric imaging, a wide physiological heterogeneity may exist within the field-of-view. In addition to the 2T model, we also considered the one-tissue (1T) model and zero-tissue (0T) models ((Fig. 1A and Table 1) – the 0T model is more suitable for those voxels containing only blood. The 1T model is equivalent to the 2T model with $k_3 = 0$, implying the phosphorylation process can be neglected when k_3 is small and

the data is noisy. The 0T model is a special case of the 1T model with $K_1 = 0$. The best model was chosen for each voxel j from a set of candidate models (0T, 1T, 2T in Table 1) according to the minimum Akaike information criteria (AIC),

$$l_j = argmin_l \ AIC_j(l), \quad (8)$$

where $\mathrm{AIC}_j(l)$ denotes the AIC of model order l ($l = 0, 1, 2$) for fitting the TAC at voxel j. The AIC with correction for a small number of frames is calculated by *(27)*,

$$\mathrm{AIC} = M \ln(RSS/M) + 2n + 2n(n+1)/(M-n-1), \quad (9)$$

where RSS is calculated using Eq. (7) for a specific model and n denotes the total number of unknown parameters in the model. A lower AIC value indicates a better model *(27)*.

Parametric Imaging with Kernel Smoothing. Voxel-wise implementation of compartmental modeling leads to the generation of parametric images of tracer kinetics, which usually suffers from high noise in voxels. The kernel method (*28*) was applied here as post-reconstruction smoothing to reduce noise in the dynamic images, which is also equivalent to nonlocal means smoothing (*28*). Fundamentally, it rests upon deriving, for each patient dataset, a kernel matrix built from four consecutive composite frames of 5 minutes, 15 minutes, 20 minutes, and 20 minutes, respectively. For each voxel, k-nearest neighbors with k=50 was constructed in a cubic 9×9×9 voxel space. More details of the method can be found in (*28*). The same kernel matrix was also applied to the parametric images for further noise suppression.

Statistical Analysis

Statistical data analysis was mainly conducted for demonstrating the impact of time-delay correction and model selection. To evaluate the effect of time-delay correction, linear regression analysis and group comparison were performed for different kinetic parameters of lesions using the paired student's t-test and Wilcoxon signed-rank test. A p value of less than 0.05 was considered statistically significant. For assessing the impact of model selection, artifacts in the K_i parametric images were identified visually in blood regions. AIC was calculated to indicate a potential overfitting of the blood TACs.

RESULTS

Patient Characteristics and Image Data

Table 2 lists the characteristics of the study subjects. All dynamic scans of the five healthy subjects and five cancer patients were successful. Nineteen lesions were identified on the SUV images of the cancer patients. Supplemental

Fig. 2 shows the dynamic FDG-PET images and regional TACs for two patients with cancer. The two patients shared a similar TAC shape for the brain and liver TACs but the TACs of the lesions are very different.

Table 2. Characteristics of subjects included in this study

Subject	Age (years)	Sex	BMI (kg/m^2)	Blood glucose level (mg/dL)	Fasting (hours)	Disease	Initial Therapy
1	78	M	24.4	101	11	Healthy	N/A
2	26	M	33.8	77	6	Healthy	N/A
3	50	M	27.2	94	12	Healthy	N/A
4	51	F	24.2	93	12	Healthy	N/A
5	62	M	29.5	92	12	Healthy	N/A
6	65	M	32.0	154	12	CC RCC Grade 2	Partial nephrectomy
7	62	M	26.3	84	8	CC RCC Grade 4	Radical nephrectomy
8	65	M	25.3	65	20	CC RCC Grade 3	Radical nephrectomy
9	76	M	20.1	128	10	CC RCC Grade 2	Radical nephrectomy
10	70	M	24.3	131	11	High-grade TCC	Radical cystectomy

CC RCC = clear cell renal cell carcinoma; TCC = transitional cell carcinoma; N/A=not applicable.
All cancer patients had stage IV disease. Fuhrman grade was used.

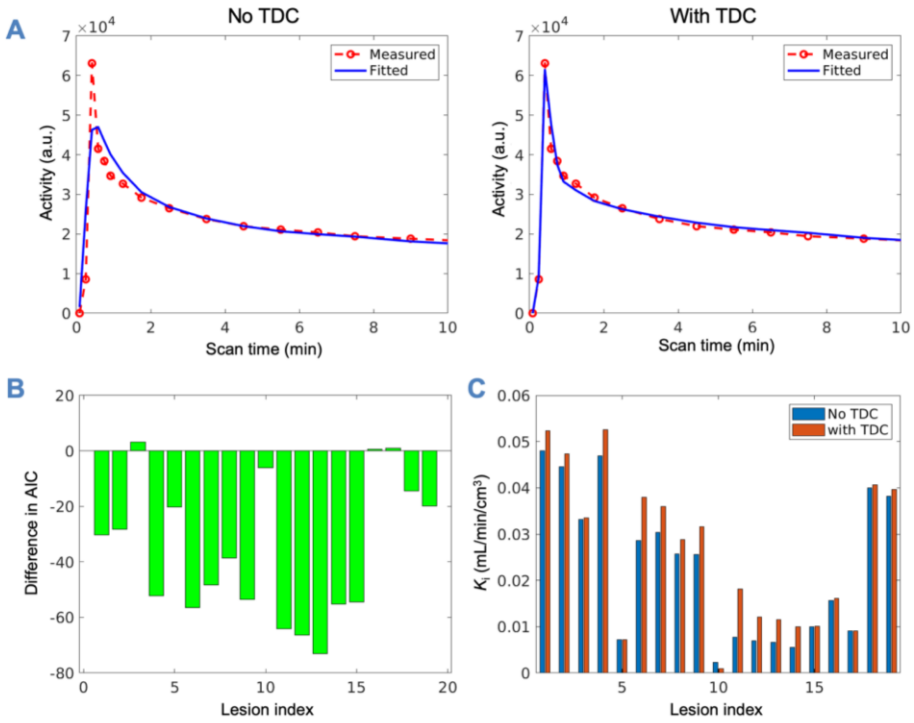

FIGURE 2. Illustration of time delay and its impact on lesion TAC fitting and kinetic quantification. (A) fitting of a liver lesion TAC with no time-delay correction (TDC) and with time-delay jointly estimated; (B) the Akaike information criteria (AIC) difference between the 2T models with and without TDC for TAC fitting in 19 lesions; (C) comparison of K_i values for individual lesions.

Effect of Time Delay Correction (TDC)

Fig. 2 shows the results of applying TDC by joint estimation to fit lesion TACs using the 2T model. The TDC resulted in an improvement in fitting the lesion TAC, particularly in the early phase where the peak is. The improved fit is further evidenced by a statistical quality evaluation using AIC in the lesions (Fig. 2B). Lower AIC was achieved by the TDC in most of the lesions. The individual lesion K_i values by the two approaches are shown in Fig. 2C. Generally, K_i became higher after TDC. The percent change in K_i and K_1 was further plotted against the fractional blood volume v_b in supplemental Fig. 3. As v_b increases, the difference in the two approaches becomes larger for both K_i and K_1.

Table 3. Mean and standard deviation of lesion kinetic parameters estimated by the 2T model with and without time-delay correction. The paired t test and Wilcoxon signed-rank test were both used for calculating p value.

	No delay correction	With delay correction	p value of paired t test	p value of paired signed-rank test
t_d (s)	0	7±5	0.0001	0.0008
v_b (mL/cm^3)	0.027±0.053	0.232±0.181	0.0002	0.0002
K_1 (mL/min/cm^3)	0.974±0.814	0.331±0.383	0.0017	0.0002
K_i (mL/min/cm^3)	0.023±0.016	0.026±0.017	0.0003	0.0005
V_0 (mL/cm^3)	0.420±0.267	0.380±0.221	0.0161	0.0123

Table 3 summarizes the kinetic results estimated by the two approaches (i.e., with and without TDC) in all the lesions. The time delay was 7±5 s (range: -2s - 18s), which is significantly different from zero as indicated by the small p value of statistical tests. TDC led to much higher v_b and appreciably lower K_1 estimates ($p<0.002$). Although the mean and standard deviation of K_i in the pooled analysis only had a small difference between the two approaches, the paired statistical tests show TDC had a statistically significant effect ($p\leq0.0005$) on K_i estimation, as reflected by the pairwise changes shown in Fig. 2C and supplemental Fig. 3. The impact on V_0 was also statistically significant ($p<0.02$).

Examples of parametric images of different kinetic parameters are shown in Fig. 3 for one cancer patient. Without TDC, the v_b image did not show all the vasculature, especially in the legs where the time delay was large. The K_1 image became clearer after the TDC because the vasculature disappeared in this image. Fig. 4 further shows the

estimated time delay map and K_i images. Lesions were less visible with low K_i values if no TDC was implemented; most of the lesions were enhanced with a higher value after TDC.

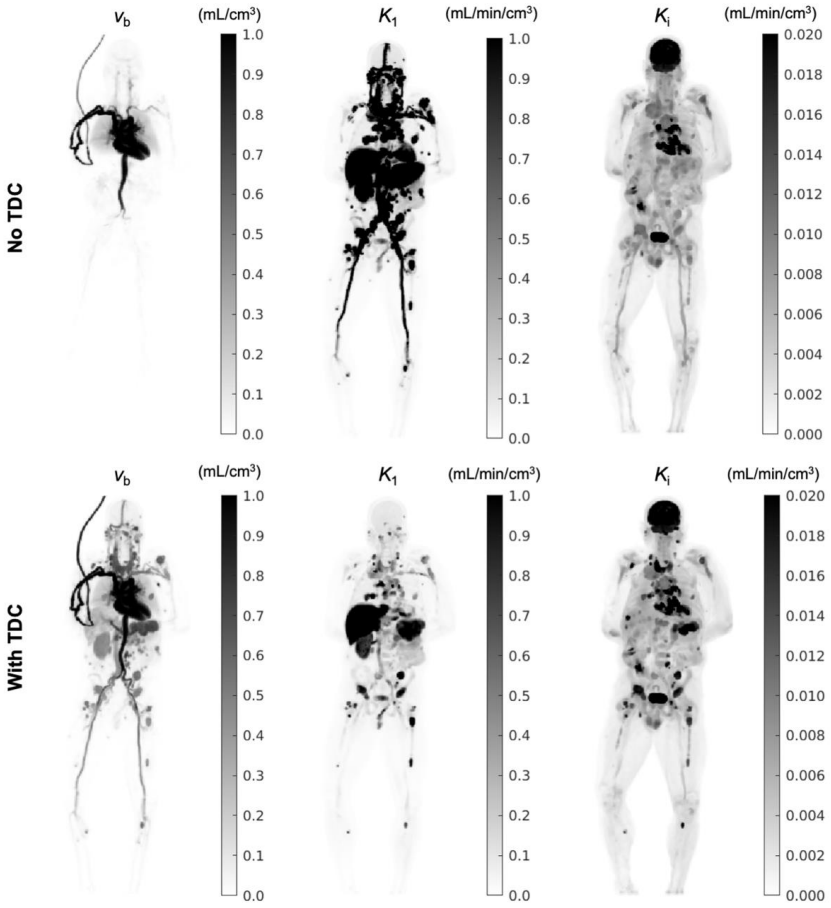

FIGURE 3. Demonstration of parametric imaging using the 2T model with and without time-delay correction (TDC) for a cancer patient. Shown are maximum intensity projection maps for v_b, K_1 and K_i.

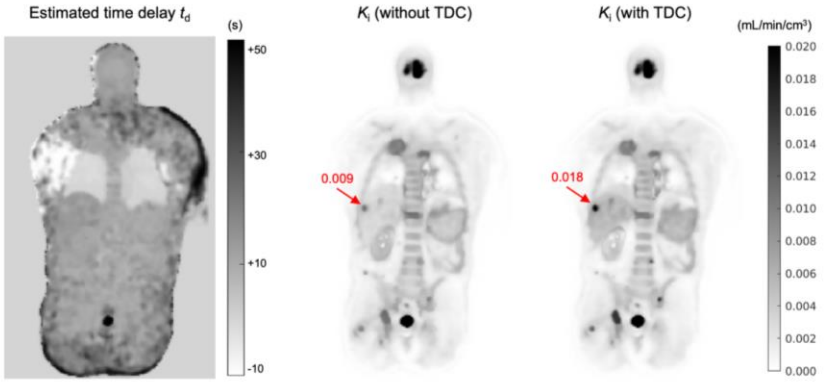

FIGURE 4. Coronal plane of the estimated time delay t_d map and K_i parametric images with and without time-delay correction (TDC) for a cancer patient. Arrows point to a liver lesion.

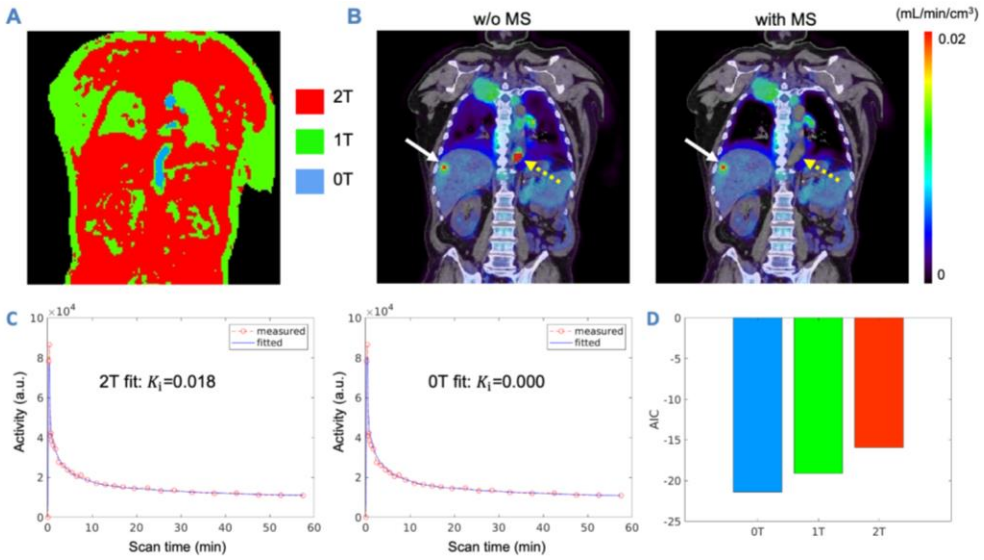

FIGURE 5. Evaluation of the impact of model selection (MS). (A) distribution map of different kinetic models (0T, 1T, 2T); (B) parametric image of K_i (overlaid on the CT images) by the 2T model with and without (w/o) voxel-wise MS. Solid arrows point to potential lesions and dashed arrows point to blood voxels in the descending aorta; (C) a blood TAC fitted with the 2T and 0T models; (D) AIC values of three models (0T, 1T, 2T).

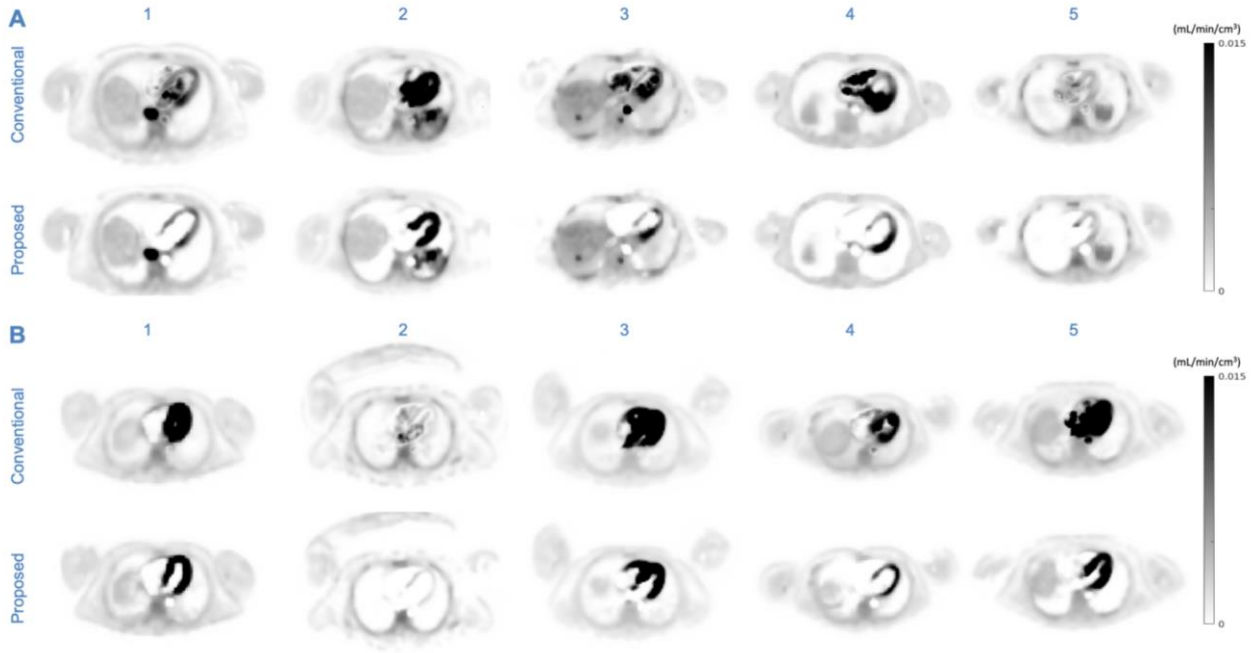

FIGURE 6. Comparison of FDG K_i parametric images generated by the conventional 2T model (with TDC) and the proposed approach that includes model selection and TDC in (A) five patients with cancer and (B) five healthy subjects.

Effect of Voxel-wise Model Selection

Fig. 5A shows the map of the model order (0T, 1T, 2T) selected for individual voxels for a cancer patient scan. Most of the body parts such as soft tissues followed the 2T model, while the lungs and skin favored the 1T model

according to AIC. Vascular regions (e.g., the heart chambers and arteries) followed the 0T model. All the lesions followed the 2T model. The parametric image of K_i generated using a single 2T model (Fig. 5B) contains a suspicious hot spot of a high K_i value. It disappeared after applying voxel-wise model selection. Fig. 5C demonstrates that both the 2T and 0T models fitted the TAC well but the resulting K_i values were very different (0.018 versus 0.0 mL/min/cm^3). The AICs of different fits by 0T, 1T, and 2T are compared in Fig. 5D. It indicates 0T was the best model for fitting the blood TAC, while the 2T model overfitted the TAC and resulted in a falsely high value of K_i.

Fig. 6 shows the comparison of the conventional single 2T model (with TDC) to the proposed method (with model selection and TDC) for parametric imaging of K_i at the level of the heart in all the ten subjects. The conventional method resulted in artificially high K_i values in some voxels primarily containing blood. The myocardium was also difficult to visualize in each patient scan. In comparison, the proposed method largely removed those artifacts and appropriate model selection leads to clear visualization of the myocardium in all the subjects.

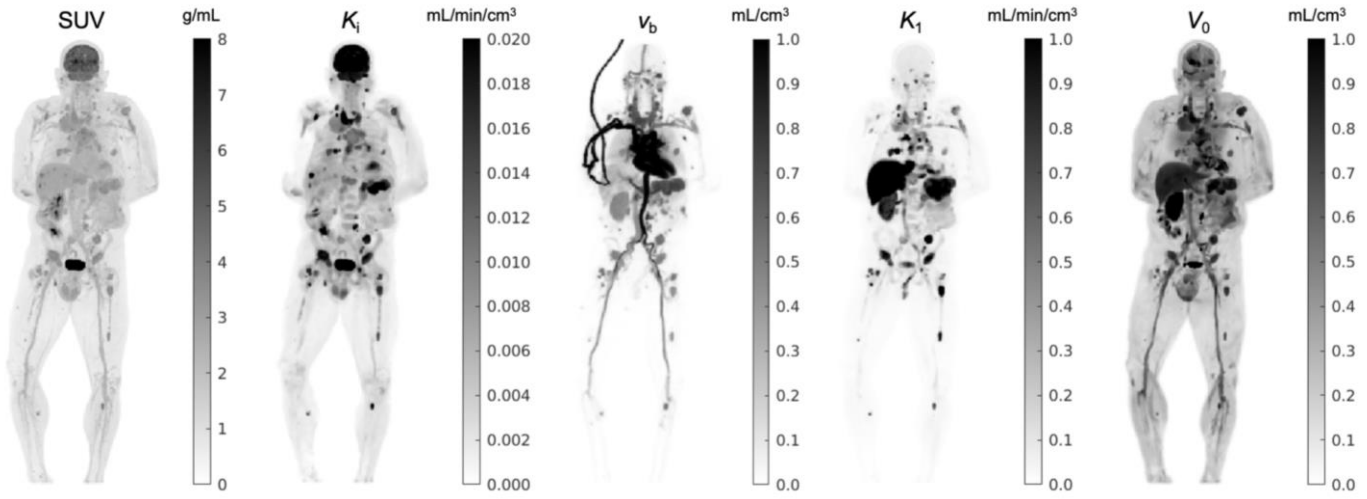

FIGURE 7. Comparison of standard SUV image with parametric images of FDG influx rate K_i, fractional blood volume v_b, FDG delivery rate K_1 and volume of distribution V_0 images of a cancer patient. Shown are maximum intensity projection maps.

Demonstration of multiparametric images

With the improved voxel-wise modeling strategy, we show parametric images for a range of kinetic parameters, including v_b, K_1, K_i and V_0 for one cancer patient in Fig. 7 and for one healthy subject in supplemental Fig. 4. The SUV images at 60 minutes post injection are also included. While the K_i and SUV images share similar information in most of the patients, the v_b, K_1 and V_0 images demonstrate very different spatial patterns in the body, thus providing

complementary information to that provided by SUV. Supplemental Fig. 5 demonstrates that parametric images can be potentially more useful than SUV for liver tumor imaging and brain tumor imaging.

DISCUSSION

In this paper, we evaluated a voxel-wise strategy for total-body FDG-PET parametric imaging using compartmental modeling. Time delay correction through joint estimation during TAC fitting was found to be significant (Fig 2) and had a high impact on quantification and parametric imaging of v_b and K_1 (Table 3, Fig. 3). The impact on K_i was of lesser extent when v_b was small but became higher as v_b increased (Fig. 4, supplemental Fig. 3). Dispersion correction was not explicitly included in this study, but the incorporation of v_b may account for the potential dispersion effect in part (*29*). The v_b values of lesions estimated in this study were relatively high ($0.23\pm0.18 mL/cm^3$), which likely reflects that most patients had clear-cell renal cell carcinoma that tends to be highly vascular (*30*). It is also perhaps because v_b is more like a method parameter than being quantitative given it also accounts for the dispersion effect.

Our study also found the standard 2T model led to artificially high values in the K_i image in those voxels primarily containing blood. This was caused by overfitting of the TACs that better follow the 0T model or 1T model, as indicated by the AIC comparison (Fig. 5). We addressed this problem by applying voxel-wise model selection using AIC. The method led to clear visualization of the myocardium, while the standard model did not (Fig. 6). Note that the AIC-based model selection is driven by statistical fit quality evaluation and cannot be over-interpretated physiologically. For example, the choice of 1T over 2T does not indicate the nonexistence of phosphorylation but suggests k_3 can be neglected when the data is noisy. As an alternative to AIC, other approaches are also possible by applying sparsity constraints to kinetic parameters or using sparse spectral analysis (*31*). In addition, factor analysis (e.g., (*32*)) and mixture models (e.g., (*33*)) could also be advantageous to explore in total-body parametric imaging (*34*).

As the first step for demonstrating a workable modeling strategy, we only considered the irreversible 2T model. This model is appropriate when the dephosphorylation process is negligible during the one-hour dynamic scan time. However, the reversible 2T model (with $k_4>0$) can be more appropriate for kinetic quantification of organs such as the liver (*35*) and myocardium (*36*). The liver and lungs also receive dual blood supplies and require modeling of their dual-blood input function for accurate kinetic quantification. These aspects were not addressed in this study. Motion correction may also further improve the quantification performance. Implementation of these more complex models in total-body parametric imaging is a part of our ongoing effort.

The focus of this paper was mainly on the methodological implementation for multiparametric imaging using compartmental modeling. Due to the page limit, the benefits of parametric images have not been directly compared to the SUV images (other than supplemental Fig. 5) and the parametric images determined from the linear Patlak plot (*5*,*14*,*37*). In general, multiparametric imaging with compartmental modeling does not only generate K_i and V_0 but can also provide other micro kinetic parameters including v_b and K_1 (Fig. 7) that go beyond what the Patlak method can offer. Exploring the potential benefits of these multiparametric images will be reported in future work.

This study has several other limitations. The temporal sampling rate for early dynamic scanning was relatively limited (10 s/frame), but was a reasonable choice based on our preliminary study as shown in supplemental Fig. 6. Within this context, the time delay t_d is mainly a method parameter that is coarsely estimated. Optimal sampling (trade-off between temporal resolution and voxel noise level) and the effect on kinetic quantification remain to be further investigated. In addition, the number of studied subjects was relatively small, and the study did not have a reference or outcome measure to evaluate the impact of kinetic quantification. The studied cancer type was also limited to genitourinary cancer. It will be worth evaluating the proposed kinetic modeling strategies in other cancers. Future studies will take these aspects into account.

CONCLUSIONS

We successfully conducted total-body PET multiparametric imaging using compartmental modeling for the dynamic FDG-PET data acquired on the uEXPLORER system in both healthy subjects and cancer patients. Time delay correction led to improved lesion TAC fitting, physiologically more consistent vasculature in the v_b image, and generally higher K_i in lesions especially when v_b was large. Voxel-wise model selection reduced artifacts in the K_i parametric images and led to clearer visualization of the myocardium. Both the modeling of time delay of the blood input function and model selection are necessary for accurate total-body multiparametric imaging.

DISCLOSURE

UC Davis has a revenue-sharing agreement with United Imaging Healthcare. RDB, SRC and GBW are investigators on a research grant funded by United Imaging Healthcare. This work is supported in part by NIH grant K12 CA138464, R01 CA206187, UC Cancer Research Coordinating Committee Grant (CRN-19-585008), and a pilot grant from the

Cancer Therapeutics Program in the UC Davis Cancer Center (NIH grant P30CA093373). No other potential conflicts of interest relevant to this article exist.

ACKNOLEDGEMENTS

We acknowledge the contributions of team members in the EXLORER Molecular Imaging Center, UC Davis.

KEY POINTS

QUESTION: Is it feasible to perform multiparametric imaging with compartmental modeling in total-body dynamic PET of cancer?

PERTINENT FINDINGS: Voxel-wise modeling of the time delay of the blood input function and model selection are necessary for accurate total-body multiparametric imaging.

IMPLICATIONS FOR PATIENT CARE: Total-body dynamic PET can enable single-tracer multiparametric imaging that may be further explored to improve tumor detection and treatment response assessment.

REFERENCES

1. Morris ED, Endres CJ, Schmidt KC, Christian BT, Muzic RF, Fisher RE. Kinetic modeling in positron emission tomography. In: Wermick MN, JN A, eds. *Emission Tomography: The Fundamentals of PET and SPECT*: Elsevier Inc.; 2004:499-540.

2. Gallezot JD, Lu YH, Naganawa M, Carson RE. Parametric Imaging With PET and SPECT. *IEEE Transactions on Radiation and Plasma Medical Sciences.* 2020;4:1-23.

3. Wang G, Rahmim A, Gunn RN. PET Parametric Imaging: Past, Present, and Future. *IEEE Transactions on Radiation and Plasma Medical Sciences.* 2020;4:663 – 675.

4. Dimitrakopoulou-Strauss A, Pan LY, Sachpekidis C. Kinetic modeling and parametric imaging with dynamic PET for oncological applications: general considerations, current clinical applications, and future perspectives. *European Journal of Nuclear Medicine and Molecular Imaging.* 2021;48:21-39.

5. Rahmim A, Lodge MA, Karakatsanis NA, et al. Dynamic whole-body PET imaging: principles, potentials and applications. *European Journal of Nuclear Medicine and Molecular Imaging.* 2019;46:501-518.

6. Karakatsanis NA, Lodge MA, Tahari AK, Zhou Y, Wahl RL, Rahmim A. Dynamic whole body PET parametric imaging: I. Concept, acquisition protocol optimization and clinical application. *Phys Med Bio.* 2013; 58:7391-7418

7. Hu JC, Panin V, Smith AM, et al. Design and Implementation of Automated Clinical Whole Body Parametric PET With Continuous Bed Motion. *IEEE Transactions on Radiation and Plasma Medical Sciences.* 2020;4:696-707.

8. Cherry SR, Jones T, Karp JS, Qi J, Moses WW, Badawi RD. Total-body PET: Maximizing sensitivity to create new opportunities for clinical research and patient care. *Journal of Nuclear Medicine.* 2018;59:3-12.

9. Badawi RD, Shi H, Hu P, et al. First human imaging studies with the EXPLORER total-body PET scanner. *Journal of Nuclear Medicine.* 2019;60:299-303.

10. Spencer BA, Berg E, Schmall JP, et al. Performance Evaluation of the uEXPLORER Total-Body PET/CT Scanner Based on NEMA NU 2-2018 with Additional Tests to Characterize PET Scanners with a Long Axial Field of View. *Journal of Nuclear Medicine.* 2021;62:861-870.

11. Pantel AR, Viswanath V, Daube-Witherspoon ME, et al. PennPET Explorer: Human Imaging on a Whole-Body Imager. *Journal of Nuclear Medicine.* 2020;61:144-151.

12. Karp JS, Schmall J, Geagan M, et al. Imaging Performance of the PennPET Explorer scanner. *Journal of Nuclear Medicine.* 2018;59:222-222.

13. Alberts I, Hunermund JN, Prenosil G, et al. Clinical performance of long axial field of view PET/CT: a head-to-head intra-individual comparison of the Biograph Vision Quadra with the Biograph Vision PET/CT. *European Journal of Nuclear Medicine and Molecular Imaging.* 2021;48:2395-2404.

14. Zhang XZ, Xie ZH, Berg E, et al. Total-Body Dynamic Reconstruction and Parametric Imaging on the uEXPLORER. *Journal of Nuclear Medicine.* 2020;61:285-291.

15. Gunn RN, Lammertsma AA, Hume SP, Cunningham VJ. Parametric imaging of ligand-receptor binding in PET using a simplified reference region model. *Neuroimage.* 1997;6:279-287.

16. Boellaard R, Delgado-Bolton R, Oyen WJG, et al. FDG PET/CT: EANM procedure guidelines for tumour imaging: version 2.0. *European Journal of Nuclear Medicine and Molecular Imaging.* 2015;42:328-354.

17. Loening AM, Gambhir SS. AMIDE: a free software tool for multimodality medical image analysis. *Molecular Imaging.* 2003;2:131-137.

18. Innis RB, Cunningham VJ, Delforge J, et al. Consensus nomenclature for in vivo imaging of reversibly binding radioligands. *Journal of Cerebral Blood Flow and Metabolism.* 2007;27:1533-1539.

19. Gunn RN, Gunn SR, Cunningham VJ. Positron emission tomography compartmental models. *Journal of Cerebral Blood Flow and Metabolism.* 2001;21:635-652.

20. Iida H, Higano S, Tomura N, et al. Evaluation of regional difference of tracer appearance time in cerebral tissues using O-15 water and dynamic positron emission tomography. *Journal of Cerebral Blood Flow and Metabolism.* 1988;8:285-288.

21. Lammertsma AA, Cunningham VJ, Deiber MP, et al. Combination of dynamic and integral methods for generating reproducible functional CBF images. *Journal of Cerebral Blood Flow and Metabolism.* 1990;10:675-686.

22. Feng T, Zhao YZ, Shi HC, et al. Total-Body Quantitative Parametric Imaging of Early Kinetics of F-18-FDG. *Journal of Nuclear Medicine.* 2020;62:738-744.

23. Thiele F, Buchert R. Evaluation of non-uniform weighting in non-linear regression for pharmacokinetic neuroreceptor modelling. *Nuclear Medicine Communications.* 2008;29:179-188.

24. Winterdahl M, Munk OL, Sorensen M, Mortensen FV, Keiding S. Hepatic Blood Perfusion Measured by 3-Minute Dynamic F-18-FDG PET in Pigs. *Journal of Nuclear Medicine.* 2011;52:1119-1124.

25. Yaqub M, Boellaard R, Kropholler MA, Lammertsma AA. Optimization algorithms and weighting factors for analysis of dynamic PET studies. *Physics in Medicine and Biology.* 2006;51:4217-4232.

26. Wang G, Qi J. An Optimization Transfer Algorithm for Nonlinear Parametric Image Reconstruction From Dynamic PET Data. *IEEE Transactions on Medical Imaging.* 2012;31:1977-1988.

27. Burnham KP, Anderson DR. Multimodel inference - understanding AIC and BIC in model selection. *Sociological Methods & Research.* 2004;33:261-304.

28. Wang G, Qi J. PET image reconstruction using kernel method. *IEEE Transactions on Medical Imaging.* 2015;34:61-71.

29. Mourik JEM, van Velden FHP, Lubberink M, et al. Image derived input functions for dynamic High Resolution Research Tomograph PET brain studies. *Neuroimage.* 2008;43:676-686.

30. Chen Y, Zhang J, Dai JR, Feng XL, Lu HZ, Zhou CW. Angiogenesis of renal cell carcinoma: perfusion CT findings. *Abdominal Imaging.* 2010;35:622-628.

31. Gunn RN, Gunn SR, Turkheimer FE, Aston JAD, Cunningham TJ. Positron emission tomography compartmental models: A basis pursuit strategy for kinetic modeling. *Journal of Cerebral Blood Flow and Metabolism.* 2002;22:1425-1439.

32. Wu HM, Hoh CK, Buxton DB, et al. Quantification of myocardial blood flow using dynamic nitrogen-13-ammonia PET studies and factor analysis of dynamic structures. *Journal of Nuclear Medicine.* 1995;36:2087-2093.

33. Osullivan F. Imaging radiotracer model parameters in PET: a mixture analysis approach. *IEEE Transactions on Medical Imaging.* 1993;12:399-412.

34. Viswanath V, Chitalia R, Pantel AR, Karp JS, Mankoff DA. Analysis of Four-Dimensional Data for Total Body PET Imaging. *PET Clinics.* 2021;16:55-64.

35. Wang GB, Corwin MT, Olson KA, Badawi RD, Sarkar S. Dynamic PET of human liver inflammation: impact of kinetic modeling with optimization-derived dual-blood input function. *Physics in Medicine and Biology.* 2018;63:155004.

36. Zuo Y, Badawi RD, Foster CC, Smith T, Lopez JE, Wang G. Multiparametric Cardiac 18F-FDG PET in Humans: Kinetic Model Selection and Identifiability Analysis. *IEEE Transactions on Radiation and Plasma Medical Sciences.* 2020;4:759-767.

37. Dias AH, Pedersen MF, Danielsen H, Munk OL, Gormsen LC. Clinical feasibility and impact of fully automated multiparametric PET imaging using direct Patlak reconstruction: evaluation of 103 dynamic whole-body(18)F-FDG PET/CT scans. *European Journal of Nuclear Medicine and Molecular Imaging.* 2021;48:837-850.

Supplemental Data

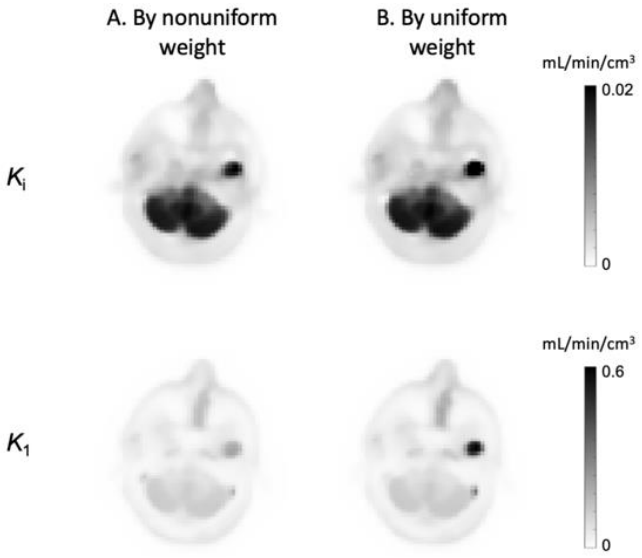

Supplemental Fig. 1: Effect of the weighting factor on parametric imaging of FDG K_i and K_1 for a patient dataset. (A) by a nonuniform weighting scheme; (B) by the uniform weight. While the K_i images by the two schemes are similar, the uniform weighting may avoid a potential underestimation of K_1 in an osteolytic lesion.

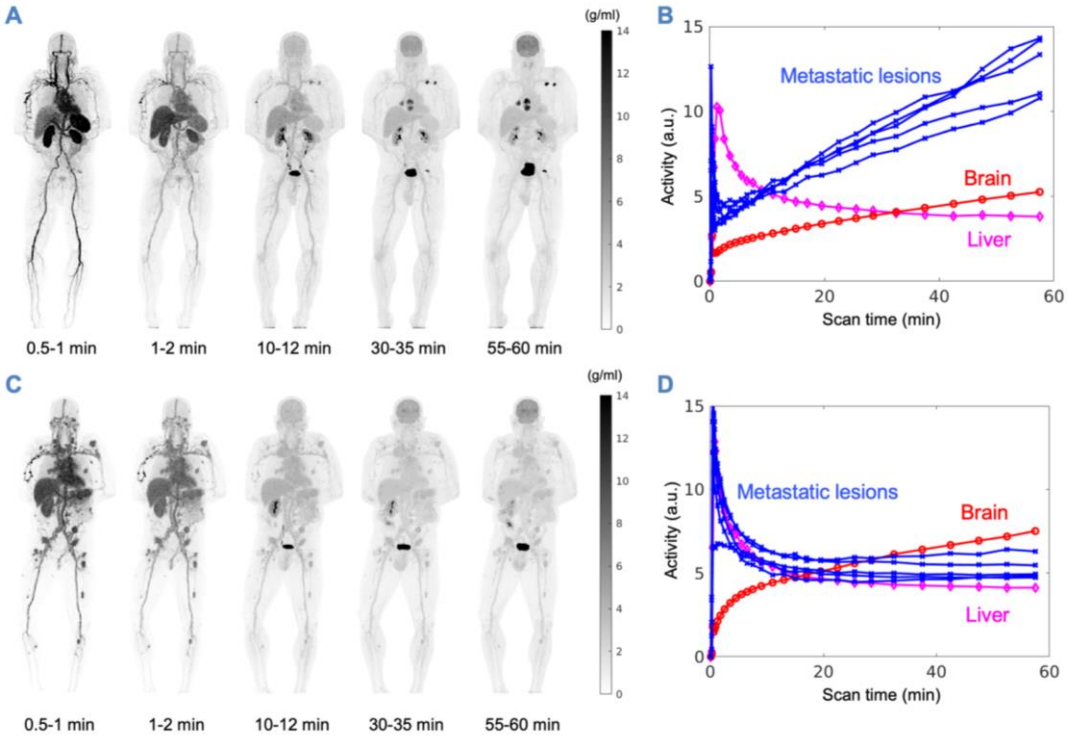

Supplemental Fig. 2: Example of total-body dynamic FDG-PET images and regional TACs of two patients with metastatic renal cancer. Shown are maximum intensity projection (MIP) images. (A) and (B) show the results from a patient with lesions demonstrating higher FDG uptake in the late phase than the early phase. (C) and (D) from another patient show higher FDG uptake in the early phase (0-2 minutes) but lower FDG uptake in the late phase (40-60 minutes) in the lesions.

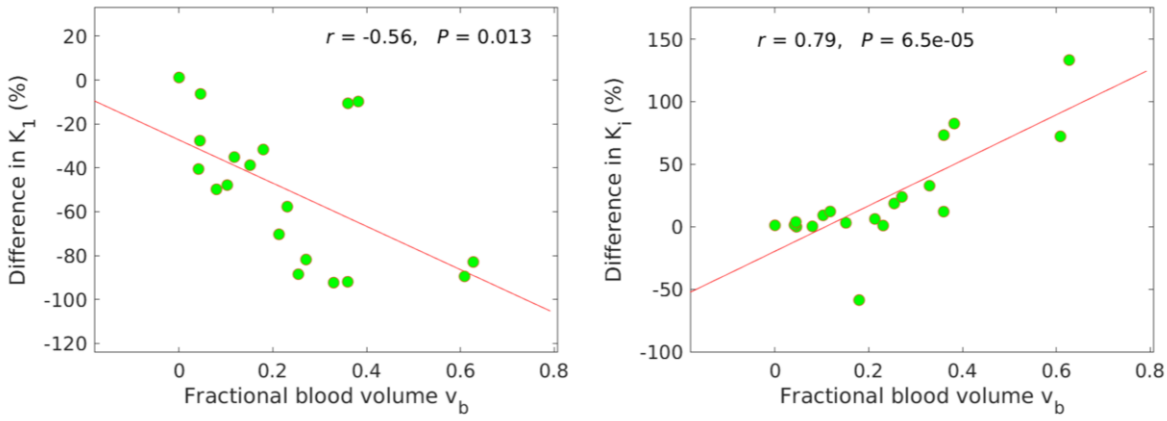

Supplemental Fig. 3: The impact of time delay correction on K_1 and K_i quantification is increased with higher fractional blood volume v_b. (A) plot of the percent change in K_1 versus the fractional blood volume v_b; (B) percent change in K_i versus v_b. The increased impact on kinetic quantification can be explained by that the vascular time course, as shown in Fig. 1B, may be estimated more accurately with time delay correction, which in turn improves the estimate of the extravascular time course significantly if v_b is large, leading to the changes in the K_1 and K_i estimates.

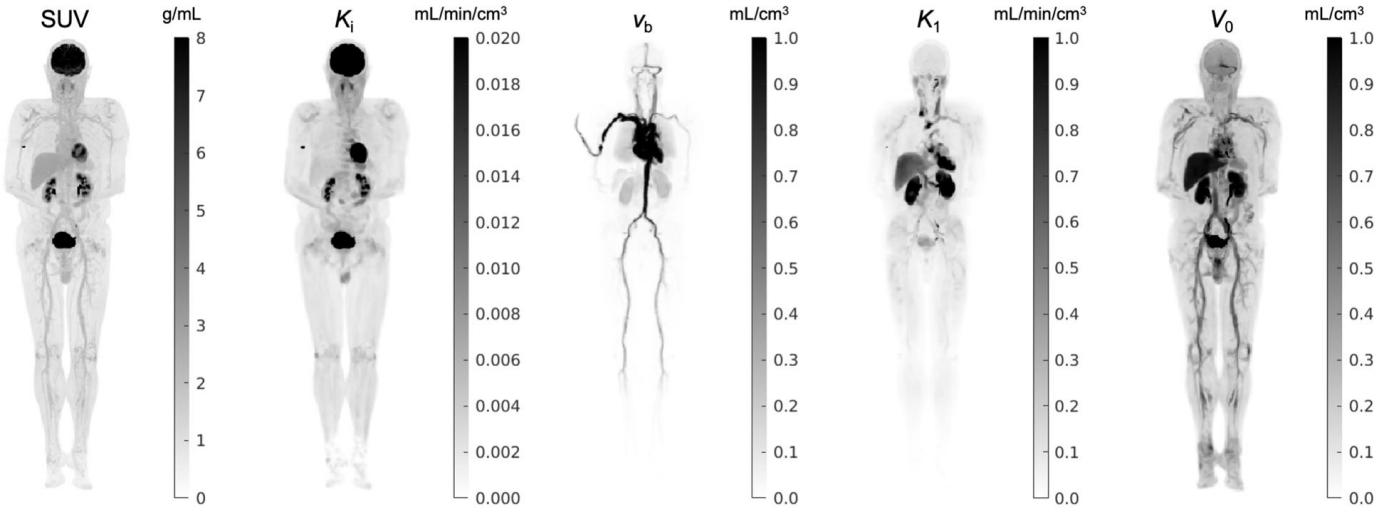

Supplemental Fig. 4: Comparison of standard SUV image with parametric images of FDG influx rate K_i, fractional blood volume v_b, FDG delivery rate K_1 and volume of distribution V_0 images of a healthy subject. Shown are maximum intensity projection maps.

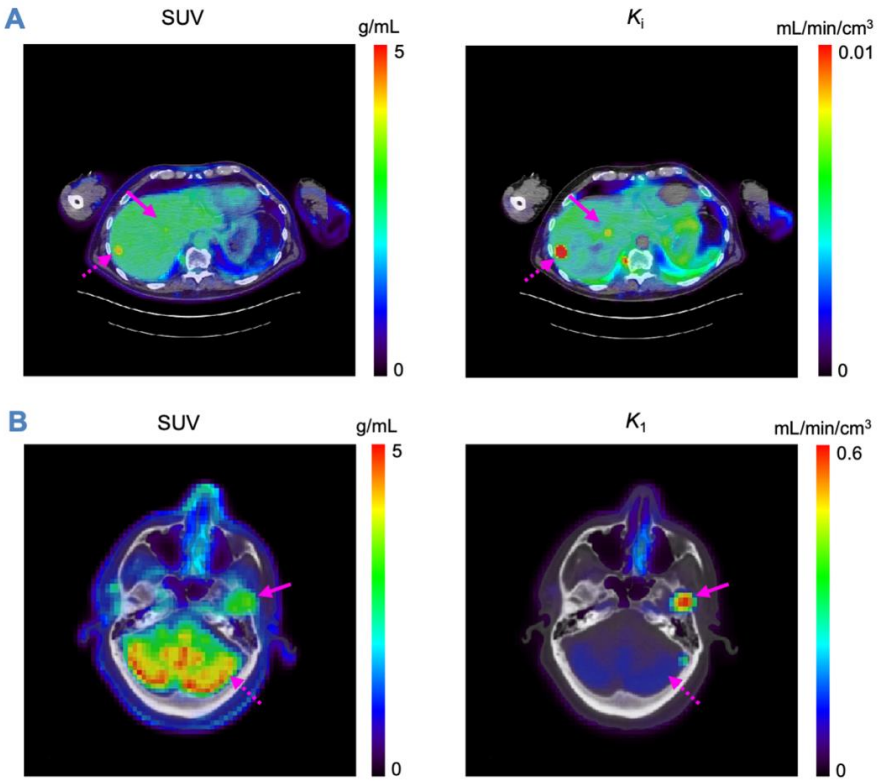

Supplemental Fig. 5: SUV and multiparametric images of a patient with cancer. (A) SUV and K_i images (overlaid on CT) of the liver; The solid and dashed arrows point to two liver lesions. Both lesions are more visible with higher contrast on the K_i image; (B) SUV and K_1 images of the head. The solid arrow points to an osteolytic lesion and the dashed arrow points to the brain. While the SUV image (and K_i image, results not shown) demonstrated high uptake in the brain background, the K_1 value was low in the brain but high in the osteolytic lesion.

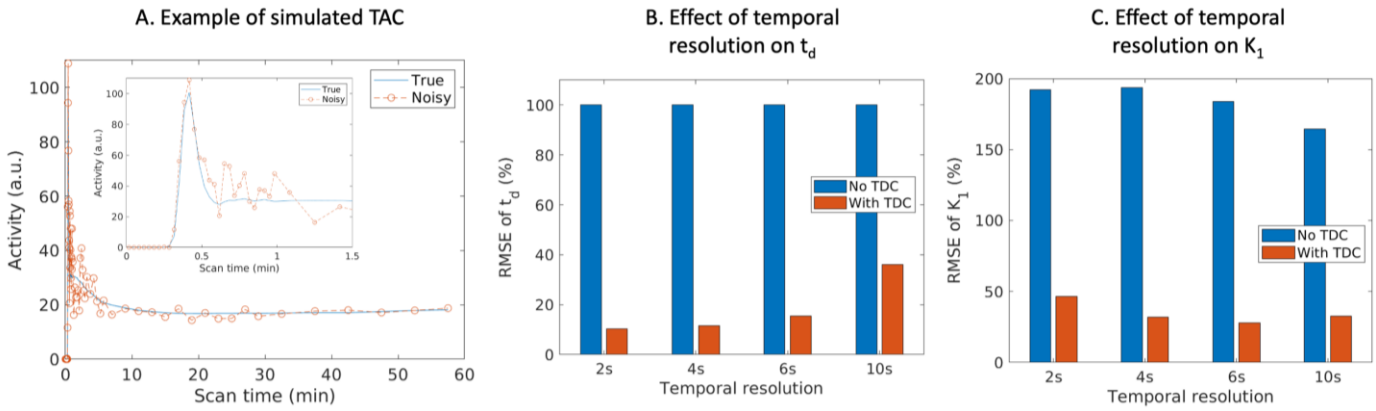

Supplemental Fig. 6: Initial simulation study of the effect of temporal resolution on estimation of time delay and FDG K_1. (A) example of simulated noisy TAC with 2s/frame in the first minute. The simulation was conducted using a lesion kinetic parameter set (t_d=7s, v_b=0.3, K_1=0.7, k_2=0.9, k_3=0.02, k_4=0) that was extracted from one patient and with 1000 noisy realizations; (B) root mean squared error (RMSE) of time delay t_d estimation. RMSE was lower with 2s/frame than with 10s/frame; (C) RMSE of FDG K_1 estimated with and without time delay correction (TDC). The RMSE became higher with 2s/frame than with 10s/frame, hypothetically because of the higher noise in the 2-s time bins and different effect on different kinetic parameters.

Graphical Abstract